

Poly-cataclasites: Implications to the Seismic Cycle

Thomas Yeo (✉ tjy.yeo@aist.go.jp)

Department of Natural History Science, Hokkaido University, 5 Chome Kita 8 Jonishi, Kita Ward,
Sapporo, Hokkaido 060-0808, Japan

Toru Takeshita

Hokkaido University

Research Article

Keywords: Poly-cataclasites, cataclastic clasts, phyllosilicate minerals, fluidisation

Posted Date: December 7th, 2020

DOI: <https://doi.org/10.21203/rs.3.rs-116257/v1>

License:  This work is licensed under a Creative Commons Attribution 4.0 International License.

[Read Full License](#)

1 Poly-cataclasites: Implications to the seismic cycle

2 **Thomas. J.Y Yeo^{1,2,*}, and Toru Takeshita^{1,‡}**

3 ¹Department of Natural History Science, Hokkaido University, 5 Chome Kita 8 Jonishi, Kita
4 Ward, Sapporo, Hokkaido 060-0808, Japan

5 ²Geological Survey of Japan, National Institute of Advanced Industrial Science and Technology
6 (AIST), AIST Tsukuba Central 7, 1-1-1 Higashi, Tsukuba, Ibaraki 305-8567, Japan

7 *TJY.YEO@aist.go.jp

8 ‡these authors contributed equally to this work

9

10 **Abstract**

11 Poly-cataclasites are rocks that have undergone multiple episodic deformational histories. These
12 rocks retained the microstructures developed from older deformational events. They are a common
13 occurrence in the Median Tectonic Line Japan and can be used to evaluate the changes in rock
14 deformational processes throughout the earthquake cycle. Based on the description of
15 mineralogical changes and the microstructures of the cataclastic clasts, we are able to establish
16 two main deformational events Microstructures of the co-seismic phase relates to the randomly
17 oriented clast developed through fluidisation. Clast that are foliated formed during the aseismic
18 phase through creeping accompanied by the precipitation of phyllosilicate minerals and the
19 consumption of feldspathic minerals. We propose that the presence of crustal fluid circulation is
20 essential in governing the poly-cataclasites deformational cycle providing insights into the
21 underlying deformational processes during the earthquake cycle.

22

23 **Introduction**

24 The Median Tectonic Line (MTL) is one of the major seismically active inland faults in Japan with
25 a long and complicated deformational history¹⁻⁵. The recurrence interval of earthquakes is
26 predicted to be in the order of 1000-3000 years^{6,7} with documents suggesting the most recent
27 rupture occurring in the 16th century⁷. Earthquakes intervals of this time scale are usually
28 controlled by earthquake deformational processes of meter to submicron scale⁸ which are not
29 obtainable from geophysical survey. Therefore, studies on exhumed fault zones that experienced
30 paleo-seismic activities are crucial to gain information on the active deformational processes⁹⁻¹¹
31 during the earthquake cycle through microstructural studies¹²⁻¹⁷. To date, fault rocks used as a
32 direct evidence of seismic activities are pseudotachylite^{18,19}, pulverisation of fault rocks²⁰⁻²² or

33 mineral reactions that suggest high temperature produced from frictional or shear heating^{11,13,23,24}.
34 Whilst, fluidisation served as an indirect evidence of earthquake activity where materials can
35 deform at a rate of mm/s to m/s of magnitude¹⁷. The microstructures for the interseismic period on
36 the other hand is usually described as the sealing of fractures through the precipitation of minerals
37 and compaction^{25,26}.

38

39 This paper attempts to related the seismic cycle phases to natural samples that had typically
40 undergone continuous polyphase deformation throughout its history,^{15,27} also known as poly-
41 cataclasites²⁸. Investigation was conducted on the exhumed fault rocks of the Ryoke Granitoids in
42 Tsukide, Mie Prefecture, Japan that has undergone direct influence from the activity of the MTL
43 from the Kashio until the Ichinokawa phase^{29,30}. Detailed descriptions of the poly-cataclasites'
44 microstructural and mineralogical heterogeneity allowed us to unravel its development with
45 respect to the seismic cycle phases³¹.

46

47 **Results**

48 The present study focuses mainly on the region seen on the map in **Fig 1**. This region has relatively
49 simple deformational history and was thought be a good location to study the early stages of the
50 MTL² as overprinting of later brittle stage (post-Ichinokawa phase) is less significant eg^{29,30}.
51 Example of poly-cataclasites shows microstructures developed at distinguished timings, where
52 aggregates that form randomly oriented cataclasite could consist of foliated clast (**Fig 2 a & b**) and
53 vice versa (**Fig 2 c & d**). The foliation of the cataclasite samples are defined by anastomosing
54 pressure solution seams (PSS) and the orientation of elongated clasts. The PSS is observed to be
55 part of the C'-S fabric indicating that they had developed through shearing (**Fig 2 e & f**).

56

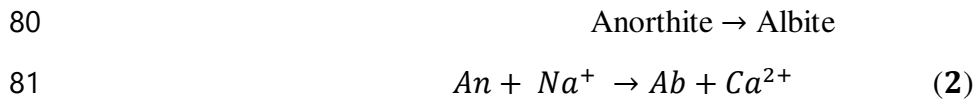
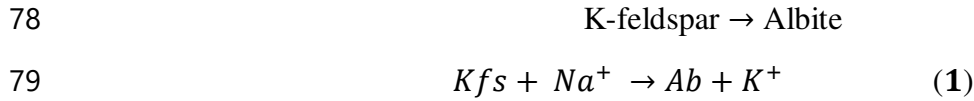
57 **Mineralogical and chemical changes**

58 The Ryoke granitoids in the field region was previously describe to have originated from two main
59 protolith namely granite and tonalite with geological distribution as seen in **Fig 1**^{29,30}. Numerous
60 brittlely deformed domains was observed in this region. XRD bulk mineralogy analysis was
61 conducted on two transects to evaluate the mineralogical changes in the damage zones within both
62 protolith. The results from **Transect 1** reveal that samples collected within fault cores indicate a
63 sharp decrease in K-feldspar percentage as oppose to an increase in clay mineral content (**Fig 3a**).

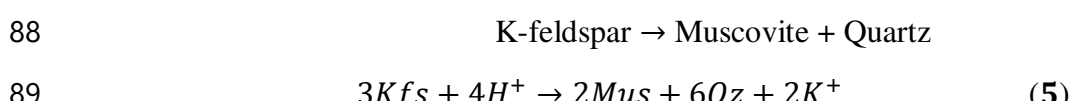
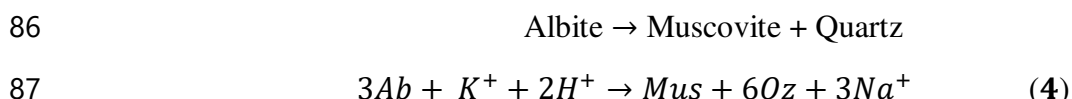
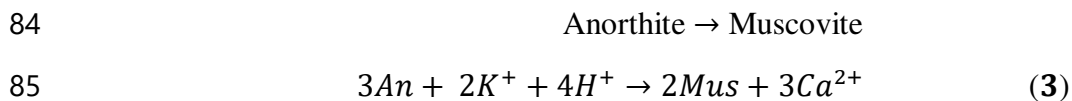
64 **Transect 2** reveals that plagioclase is reduced while illite and quartz content increases (**Fig 3b**,
 65 cf³²). Both results suggest the alteration of feldspar to clay minerals occurring at the proximity of
 66 fault cores.

67
 68 To identify the mechanism causing the decrease of K-feldspar content in preference to plagioclase
 69 within **Transect 1**, chemical mapping by SEM-EDS analysis was conducted in sample G.myl 2.
 70 **Fig 4** shows that potassium exists in the PSS and are inferred to be hosted by minerals such as
 71 muscovite or illite. Another important observation indicates that the plagioclase present are sodium
 72 rich. Conversely, the calcium was hosted mainly by carbonates. We interpret these phenomena to
 73 be a product of albitisation^{33,34} and muscovitisation^{35,36} contributed by the increase of fracture
 74 density in the damage zone leading to the enhancement of fluid flow. The reaction in the system
 75 could be summarised as follows:

76
 77 a) Albitisation:



82
 83 b) Muscovitisation:



90
 91 **Granular microstructure of the poly-cataclasites**

92 The identification of the clast's microstructures within the poly-cataclasites was performed on the
 93 traced outlines from the thin section and backscattered electron images. Clasts formed at

94 distinguished timings could be identified with dissimilar microstructures (**Fig 5**). We observed that
95 the larger clasts consist of the aggregates of smaller clast embedded within. Similar
96 microstructures are again observed in the smaller clast which suggest multi-episodic deformation.

97
98 We have simplified the repetitive structures into two distinguished categories. Based on **Fig 5** and
99 **Fig 6** the larger clast (G2) which are defined to be younger, possess a higher mean aspect ratio and
100 the clasts are identified to have a preferred orientation with increasing aspect ratio. Contrary to
101 that, the older and smaller clasts (G1) which are embedded in the G2 clasts have a smaller average
102 aspect ratio and the clasts have random orientation. The Fry's analysis (eg³⁷) was performed to
103 further quantify the distribution of the clasts (**Fig 6**). G2 clast was again observed to possess a
104 preferred distribution with a strain ellipse of an aspect ratio of 3.2. Whereas the G1 clast produced
105 a weakly deformed ellipse and again an almost random distribution.

106
107 Measurement on the grain size was performed to distinguish the spread of grain size frequency³⁸.
108 The G1 and G2 clast has a critical diameter (D_c) of 0.097 mm and 1.839 mm respectively (**Fig**
109 **7A**). Whereas the power-law exponent (β) for G1 clast is calculated to be 1.908 and 2.789 for the
110 G2 clast. This reflects that the older G1 clast has a more homogeneous spread in grain size
111 compared to the younger G2 clast

112
113 The probability of fragmented counterparts ($P(D)$) of both generations of clasts (**Fig 7B**) was
114 measured^{39,40}. G1 clast with size smaller than 10 μm are generally disregarded as their boundaries
115 have been intensely affected by pressure solution. In the case of G2 clast, it is hard to identify clast
116 of less than 100 μm . The $P(D)$ value for the G2 clast is observed to be close to 0.9 for clast
117 diameter larger than $\sim 400 \mu\text{m}$ and a decrease in $P(D)$ is only visible at clast diameter smaller than
118 $\sim 400 \mu\text{m}$. Conversely, the $P(D)$ value for the G1 shows an abrupt decrease in the $P(D)$ from 400-
119 100 μm . G1 clast with diameter smaller than 40 μm has an average $P(D)$ of >0.1 which suggest
120 potential fluidisation³⁹ as fluidisation displaces the clast randomly leading to harder detection of
121 their fragmented counterparts .

122

123 **Discussions**

124 **Effects of fluid infiltration**

125 Brittle deformation in the seismogenic zone generates fractures that would allow for the increased
126 in permeability and fluid flow causing the frictional-viscous flow⁴¹ mechanism to dominate. This
127 mechanism is crucial for two main fluid-assisted diffusive mass transfer mechanism:

128
129 (1) During cataclasis, rigid bodies of albite and quartz clasts could become interlocked as
130 deformation progresses due to volume incompatibilities. The development of the shape preferred
131 orientation in the G2 clasts and PSS shows that pressure solution occurs to facilitate the removal
132 of volume incompatible rigid materials such as quartz and feldspar at interlocking regions while
133 phyllosilicates are precipitated at the lower stress sites of the grains²⁶.

134
135 (2) Mineral alteration took place leading to albitisation and muscovitisation. The albitisation
136 process causes the alteration of plagioclase and K-feldspar into almost pure albite thus releasing
137 free K^+ and Ca^{2+} ions³³ (**Equation 1 & 2**). The muscovitisation process on the other hand would
138 result in the precipitation of muscovite and quartz by consuming the feldspars⁴² (**Equation 3, 4 &**
139 **5**). Both these reactions could act as a source of potassium required for the precipitation of the
140 white mica as PSS, while the excess calcium and silica could fill up the fractures as veins, thus
141 effectively reducing permeability and limiting further fluid influx^{36,43}.

142
143 **Evidence for seismic cycles**

144 Poly-cataclasites show evidence where episodic deformation occurred. We propose that the poly-
145 cataclasites are evidence of the seismic cycles where episodic changes in the deformation slip
146 velocity ensued. Foliations in cataclasites are often discussed to be associated with aseismic slip
147 (eg:⁴⁴⁻⁴⁷). Experimental evidences has also shown that foliations could develop from aseismic slip
148 rates (eg:^{48,49}). Frictional-viscous flow is important in maintaining the slow fault creep of the
149 aseismic slip period (eg:^{23,50}) as pressure solution can effectively avoid strain hardening in the fault
150 rocks through fluid assisted diffusion processes²⁶. During fault failure, dynamic stress could
151 increase rapidly in a short span of time¹⁰ leading to intense fragmentation, clast size reduction,
152 fluidisation or even the pulverisation of materials (eg^{10,40}). Fluidisation or inertial granular flow
153 could occur alongside with other deformational mechanism such as cataclastic flow with
154 significant enough slip rate¹³. Evidence of fluidisation are randomly oriented cataclastic clast
155 accompanied by a well-mixed distribution of grain size.

156 **Conclusions**

157 **Fig 8** summarised the development of the poly-cataclasite evolution cycle. The randomly oriented
158 G1 clasts are suggested to have develop during the period when fast slip rate occurred (eg:⁴⁸). The
159 slip rate is significantly fast to cause fluidisation to occur on the smaller clasts potentially
160 generating seismic waves¹³. Subsequent fluid flow would cause cementation of the clast, and
161 precipitation of phyllosilicates. The randomly oriented clast would be ‘locked’ into its position in
162 the newly lithified rocks. During the aseismic slip period, slip occurred and localised in the
163 phyllosilicates lamellae⁴⁴. Further pressure solutions would remove interlocking materials⁵¹ thus
164 promoting the occurrence of aseismic slip and create strongly foliated cataclasites with well-
165 rounded clasts (G2). The changes of these microstructures found within poly-cataclasites are
166 inferred to have essentially arisen from the repeated switching of co-seismic and interseismic
167 periods. These observations illustrate the fundamental link on how the evidence of the poly-
168 cataclasite deformational cycle relates to the earthquake cycle in the MTL where crustal fluid
169 circulation appears essential in the development of these poly-cataclasites

170

171 **Methods**

172 **Thin section preparation**

173 Thin section samples were made according to the XZ plane based on the principal strain axis
174 whenever possible for all samples. Here, X, Y and Z are the finite strain axes, and it is assumed
175 that the foliation is parallel to the XY-plane, and the lineation is parallel to the X-axis. The images
176 of the thin section samples were then digitalised and processed using software such as MATLAB™
177 and ImageJ. Data obtained include clast size distribution, and clast aspect ratio and orientation
178 (e.g.⁵³).

179

180 **Shape preferred orientation (SPO) and grain distribution analysis**

181 Techniques used to identify the SPO of the clast could be referred to e.g.⁵³. The shape of the
182 cataclasitic clast could be traced manually from the photographs of the XZ thin sections. The aspect
183 ratio (R_f) could then be obtained from the ImageJ software by superposing a best fitted ellipse
184 fitted onto the traced clasts. The R_f of the fitted ellipse could be defined as the ratio of the longest
185 axis (a) and shortest axis (b).

186
$$R_f = a/b \quad (6)$$

187 On the other hand, the angle ϕ is defined as the angle of the long axis (a) of the clasts relative to
 188 the reference orientation measured clockwise. The SPO could be analysed through plotting an R_f
 189 vs ϕ graph.

190
 191 The Fry's analysis was applied for the grain distribution analysis using the 2D coordinate
 192 information obtained from the best fitted ellipse mentioned above. The EllipseFit⁵⁴ software was
 193 applied for quick generation of the Fry's plot acquired from the centre point of the best fitted
 194 ellipse. The shape of the centre void on the Fry's plot represents the information on the strain and
 195 grain distributions.

196
 197 **Fractal distribution analysis**

198 The size frequency for the cataclastic clast size was analysed from the modified power function
 199 (**Equation 7**) eg ³⁸⁻⁴⁰. P represent the cumulative probability of the clast number N , with a
 200 diameter of long axis D while N_t is the total number of grains. D_c is the cut-off size with α as the
 201 parameter of cut-off sharpness and β as the power-law exponent. **Equation 7** converges to $P = 1$
 202 where $D_c > D$ and to **Equation 8** where $D_c < D$ ³⁸.

203
$$P = \frac{N}{N_t} = \left[1 + \left[\frac{D}{D_c} \right]^\alpha \right]^{-\frac{\beta}{\alpha}} \quad (7)$$

204
$$P = \left(\frac{D}{D_c} \right)^{-\beta} \quad (8)$$

205
 206 **Measure of fluidisation**

207 Methods for the quantification and identification of fluidisation are shown in **Fig 7** based on
 208 **Equation 9**^{39,40}. $P(r)$ represent the probability of detected fragmented counterparts of the
 209 cataclastic clast. It is defined by the ratio number of fragmented counterparts $N_f(r)$ to the total
 210 number of grains. A small $P(r)$ is expected to be observed in fault rocks affected by fluidisation
 211 and the opposite is true for the frictionally commuted fault materials. The clasts were observed
 212 under optical microscope in a fix area with magnification of until 10*10.

213
$$P(r) = \left(\frac{N_f(r)}{N_t(r)} \right) \quad (9)$$

215 **X-Ray Diffraction (XRD)**

216 Samples intended for bulk mineralogy identification are first grounded, powdered and was added
217 with a 20% weight percentage (wt%) of standard sample (Al_2O_3). The analysis was then
218 conducted from a 2-theta angle ($2\theta^\circ$) of 5° to 65° . The obtained results were then evaluated using
219 Profex⁵⁵ to calculate the weighted percentage of major rock forming minerals such as quartz,
220 feldspars, calcite and altered minerals such as illite and other types of clay minerals. The method
221 conducted was not able to accurately distinguish the types of clay minerals for chlorite, smectite
222 and kaolinite due to similar and overlapping peak 2-theta angle (2θ) intensity. Also, identification
223 of minerals such as illite and muscovite is also difficult due to similar reason and thus for this
224 paper, they would be referred to as only white mica. Both of these minerals are present as sericite
225 from altered products of feldspar and precipitated minerals in the PSS.

226

227 **Scanning electron microscopy (SEM) Energy Dispersive Spectroscopy (EDS)**

228 Thin section samples were mechanically polished until a $\frac{1}{4}$ μm grid size diamond paste, followed
229 by chemo-mechanical polishing using colloidal silica. The SEM was performed on carbon coated
230 samples in a JEOL JIB-4600F/HKD field-emission gun scanning electron microscope (FEG–SEM)
231 in Hokkaido University, Japan. Backscattered electron images (BEI) could be acquired from SEM
232 and were used for image analysis. For EDS analysis, a few foliated cataclasite samples were
233 selected and elemental mapping was performed to identify and determine the types of altered
234 minerals present and their relationships.

235

236 **References**

- 237 1. Shimada, K., Takagi, H. & Osawa, H. Geotectonic evolution in transpressional regime:
238 time and space relationships between mylonitization and folding in the southern Ryoke
239 belt, eastern Kii Peninsula, southwest Japan. *J. Geol. Soc. Japan* **104**, 825–844 (1998).
- 240 2. Ichikawa, K. Geohistory of the Median Tectonic Line of Southwest Japan. *Mem. Geol.*
241 *Soc. Japan* 187–212 (1980).
- 242 3. Takagi, H. Implications of mylonitic microstructures for the geotectonic evolution of the
243 Median Tectonic Line, central Japan. *J. Struct. Geol.* **8**, 3–14 (1986).
- 244 4. Kubota, Y. & Takeshita, T. Paleocene large-scale normal faulting along the Median
245 Tectonic Line, western Shikoku, Japan. *Isl. Arc* **17**, 129–151 (2008).

- 246 5. Kubota, Y., Takeshita, T., Yagi, K. & Itaya, T. Kinematic Analyses and Radiometric
247 Dating of the Large-Scale Paleogene Two-Phase Faulting Along the Median Tectonic
248 Line, Southwest Japan. *Tectonics* **39**, (2020).
- 249 6. Ikeda, M. *et al.* Tectonic model and fault segmentation of the Median Tectonic Line active
250 fault system on Shikoku, Japan. *Tectonics* **28**, n/a-n/a (2009).
- 251 7. Tsutsumi, H. & Okada, A. Segmentation and Holocene surface faulting on the Median
252 Tectonic Line, southwest Japan. *J. Geophys. Res. B Solid Earth* **101**, 5855–5871 (1996).
- 253 8. *Fault-Zone Properties and Earthquake Rupture Dynamics*, (ed. Fukuyama, E) *Volume 94*.
254 (Academic Press).
- 255 9. Wintsch, R. P. & Yeh, M. W. Oscillating brittle and viscous behavior through the
256 earthquake cycle in the Red River Shear Zone: Monitoring flips between reaction and
257 textural softening and hardening. *Tectonophysics* **587**, 46–62 (2013).
- 258 10. Reches, Z. & Dewers, T. A. Gouge formation by dynamic pulverization during earthquake
259 rupture. *Earth Planet. Sci. Lett.* **235**, 361–374 (2005).
- 260 11. Ishikawa, T. *et al.* Geochemical and mineralogical characteristics of fault gouge in the
261 Median Tectonic Line, Japan: Evidence for earthquake slip. *Earth, Planets Sp.* (2014)
262 doi:10.1186/1880-5981-66-36.
- 263 12. Sibson, R. H. Fault rocks and fault mechanisms *Journal of the Geological Society. J.*
264 *Geol. Soc. London.* **133**, 191–213 (1977).
- 265 13. Rowe, C. D. & Griffith, W. A. Do faults preserve a record of seismic slip: A second
266 opinion. *Journal of Structural Geology* vol. 78 1–26 (2015).
- 267 14. Scholz, C. H. *The Mechanics of Earthquakes and Faulting. The Mechanics of*
268 *Earthquakes and Faulting* (Cambridge University Press, 2019).
269 doi:10.1017/9781316681473.
- 270 15. Masoch, S., Fondriest, M., Preto, N., Secco, M. & Di Toro, G. Seismic cycle recorded in
271 cockade-bearing faults (Col de Teghime, Alpine Corsica). *J. Struct. Geol.* **129**, 103889
272 (2019).
- 273 16. Collettini, C., Niemeijer, A., Viti, C. & Marone, C. Fault zone fabric and fault weakness.
274 *Nature* **462**, 907–910 (2009).
- 275 17. Berger, A. & Herwegh, M. Cockade structures as a paleo-earthquake proxy in upper
276 crustal hydrothermal systems. *Sci. Rep.* **9**, 1–9 (2019).

- 277 18. Sibson, R. H. Generation of Pseudotachylyte by Ancient Seismic Faulting. *Geophys. J. R.*
278 *Astron. Soc.* **43**, 775–794 (1975).
- 279 19. Cowan, D. S. Do faults preserve a record of seismic slip? A field geologist’s opinion. *J.*
280 *Struct. Geol.* **21**, 995–1001 (1999).
- 281 20. Xu, S. & Ben-Zion, Y. Numerical and theoretical analyses of in-plane dynamic rupture on
282 a frictional interface and off-fault yielding patterns at different scale. *Geophys. J. Int.* **193**,
283 304–320 (2013).
- 284 21. Mitchell, T. M., Ben-Zion, Y. & Shimamoto, T. Pulverized fault rocks and damage
285 asymmetry along the Arima-Takatsuki Tectonic Line, Japan. *Earth Planet. Sci. Lett.* **308**,
286 284–297 (2011).
- 287 22. Dor, O., Rockwell, T. K. & Ben-Zion, Y. Geological observations of damage asymmetry
288 in the structure of the San Jacinto, San Andreas and Punchbowl faults in Southern
289 California: A possible indicator for preferred rupture propagation direction. *Pure Appl.*
290 *Geophys.* **163**, 301–349 (2006).
- 291 23. Bürgmann, R. The geophysics, geology and mechanics of slow fault slip. *Earth Planet.*
292 *Sci. Lett.* **495**, 112–134 (2018).
- 293 24. Ishikawa, T. *et al.* Coseismic fluid–rock interactions at high temperatures in the
294 Chelungpu fault. *Nat. Geosci.* **1**, 679–683 (2008).
- 295 25. Gratier, J.-P., Favreau, P. & Renard, F. Modeling fluid transfer along California faults
296 when integrating pressure solution crack sealing and compaction processes. *J. Geophys.*
297 *Res. Solid Earth* **108**, (2003).
- 298 26. Gratier, J. P. *et al.* Aseismic sliding of active faults by pressure solution creep: Evidence
299 from the San Andreas fault observatory at Depth. *Geology* **39**, 1131–1134 (2011).
- 300 27. Rowe, C. D., Meneghini, F. & Casey Moore, J. Textural record of the seismic cycle:
301 Strain-rate variation in an ancient subduction thrust. *Geol. Soc. Spec. Publ.* **359**, 77–95
302 (2011).
- 303 28. Higgins, M. . Cataclastic Rocks. *U.S. Geol. Surv. Prof. Pap.* **687**, 97 (1971).
- 304 29. Czertowicz, T. A. *et al.* The architecture of long-lived fault zones : insights from
305 microstructure and quartz lattice-preferred orientations in mylonites of the Median
306 Tectonic Line , SW Japan. *Prog. Earth Planet. Sci.* **6**, (2019).
- 307 30. Bui, V. D. Development of the Median Tectonic Line fault zone, Mie Prefecture,

- 308 southwest Japan: Strain localization and softening. (Hokkaido Univeristy, 2019).
- 309 31. Di Toro, G., Mitterpergher, S., Ferri, F., Mitchell, T. M. & Pennacchioni, G. The
310 contribution of structural geology, experimental rock deformation and numerical
311 modelling to an improved understanding of the seismic cycle. Preface to the Special
312 Volume ‘Physico-chemical processes in seismic faults’. *J. Struct. Geol.* **38**, 3–10 (2012).
- 313 32. Kaneko, Y., Takeshita, T. & Watanabe, Y. *Alteration Reaction and Mass Transfer via*
314 *Fluids with Progress of Fracturing along the Median Tectonic Line, Mie Prefecture,*
315 *Southwest Japan. Evolutionary Models of Convergent Margins : Origin of Their Diversity*
316 (IntechOpen, 2017). doi:10.5772/63702.
- 317 33. Kaur, P. *et al.* Two-Stage, Extreme Albitization of A-type Granites from Rajasthan, NW
318 India. *J. Petrol.* **53**, 919–948 (2012).
- 319 34. Spruzeniece, L. & Piazzolo, S. Strain localization in brittle-ductile shear zones: Fluid-
320 abundant vs. fluid-limited conditions (an example from Wyangala area, Australia). *Solid*
321 *Earth* **6**, 881–901 (2015).
- 322 35. Wibberley, C. Are feldspar-to-mica reactions necessarily reaction-softening processes in
323 fault zones? *J. Struct. Geol.* **21**, 1219–1227 (1999).
- 324 36. Cavailhes, T. *et al.* Phyllosilicates formation in faults rocks: Implications for dormant
325 fault-sealing potential and fault strength in the upper crust. *Geophys. Res. Lett.* **40**, 4272–
326 4278 (2013).
- 327 37. Fry, N. Random point distributions and strain measurement in rocks. *Tectonophysics* **60**,
328 89–105 (1979).
- 329 38. Otsuki, K. An empirical evolution law of fractal size frequency of fault population and its
330 similarity law. *Geophys. Res. Lett.* **25**, 671–674 (1998).
- 331 39. Otsuki, K., Monzawa, N. & Nagase, T. Fluidization and melting of fault gouge during
332 seismic slip: Identification in the Nojima fault zone and implications for focal earthquake
333 mechanisms. *J. Geophys. Res. Solid Earth* **108**, (2003).
- 334 40. Monzawa, N. & Otsuki, K. Comminution and fluidization of granular fault materials:
335 Implications for fault slip behavior. *Tectonophysics* **367**, 127–143 (2003).
- 336 41. Bos, B., Peach, C. J. & Spiers, C. J. Frictional-viscous flow of simulated fault gouge
337 caused by the combined effects of phyllosilicates and pressure solution. *Tectonophysics*
338 **327**, 173–194 (2000).

- 339 42. Wibberley, C. A. J. & McCaig, A. M. Quantifying orthoclase and albite muscovitisation
340 sequences in fault zones. *Chem. Geol.* **165**, 181–196 (2000).
- 341 43. Cavailhes, T. *et al.* Influence of fault rock foliation on fault zone permeability : The case
342 of deeply buried arkosic sandstones (Grès d ' Annot , southeastern France). *Am. Assoc.*
343 *Pet. Geol. Bull.* (2013) doi:10.1306/03071312127.
- 344 44. Wallis, D., Lloyd, G. E., Phillips, R. J., Parsons, A. J. & Walshaw, R. D. Low effective
345 fault strength due to frictional-viscous flow in phyllonites, Karakoram Fault Zone, NW
346 India. *J. Struct. Geol.* **77**, 45–61 (2015).
- 347 45. Wintsch, R. P., Christoffersen, R. & Kronenberg, A. K. Fluid-rock reaction weakening of
348 fault zones. *J. Geophys. Res.* **100**, 13021–13032 (1995).
- 349 46. Collettini, C., Tesei, T., Scuderi, M. M., Carpenter, B. M. & Viti, C. Beyond Byerlee
350 friction, weak faults and implications for slip behavior. *Earth Planet. Sci. Lett.* **519**, 245–
351 263 (2019).
- 352 47. Jefferies, S. P. *et al.* The nature and importance of phyllonite development in crustal-scale
353 fault cores: An example from the Median Tectonic Line, Japan. *J. Struct. Geol.* **28**, 220–
354 235 (2006).
- 355 48. Niemeijer, A. R. & Spiers, C. J. Influence of phyllosilicates on fault strength in the brittle-
356 ductile transition: Insights from rock analogue experiments. *Geol. Soc. Spec. Publ.* **245**,
357 303–327 (2005).
- 358 49. Bos, B. & Spiers, C. . Experimental investigation into the microstructural and mechanical
359 evolution of phyllosilicate-bearing fault rock under conditions favouring pressure solution.
360 *J. Struct. Geol.* **23**, 1187–1202 (2001).
- 361 50. Fagereng, Å. & Den Hartog, S. A. M. Subduction megathrust creep governed by pressure
362 solution and frictional-viscous flow. *Nat. Geosci.* **10**, 51–57 (2017).
- 363 51. Chester, F. M., Friedman, M. & Logan, J. M. Foliated cataclasites. *Tectonophysics* **111**,
364 139–146 (1985).
- 365 52. Woodcock, N. H. & Mort, K. Classification of fault breccias and related fault rocks. *Geol.*
366 *Mag* **145**, 435–440 (2008).
- 367 53. Takeshita, T. & El-Fakharani, A. H. Coupled micro-faulting and pressure solution creep
368 overprinted on quartz schist deformed by intracrystalline plasticity during exhumation of
369 the Sambagawa metamorphic rocks, southwest Japan. *J. Struct. Geol.* **46**, 142–157 (2013).

- 370 54. Vollmer, F. W. *A comparison of ellipse-fitting techniques for two and three-dimensional*
371 *strain analysis, and their implementation in an integrated computer program designed for*
372 *field-based studies.* (2010).
- 373 55. Doebelin, N. & Kleeberg, R. Profex: A graphical user interface for the Rietveld
374 refinement program BGMN. *J. Appl. Crystallogr.* **48**, 1573–1580 (2015).

375

376 **Acknowledgements**

377 We are grateful to N. Shigematsu for his insightful comments. Advice for the XRD analysis from J. Kameda
378 is greatly appreciated. We also like to thank T. Nagai and Geological Survey of Japan for providing the
379 usage of analytical equipment and facilities.

380

381 **Author contributions**

382 T.Y.: Fieldwork, sample preparation, data acquisition, analysis and elaboration. T.T.: Analysis and
383 Elaboration. All authors contributed to the writing and review of the manuscript.

384

385 **Competing interests**

386 The authors declare that they have no conflict of interest.

387

388 **Figure Legend**

389 Figure 1 (a) Geological map showing the lithological distribution and location of samples collected
390 in the MTL fault zone. Black and red T-symbols represent the mylonitic foliation and the planar
391 orientation of the MTL respectively. Contours are spaced with a 20 m interval. (b) Map indicating
392 the location of the field region (Source: Geological Survey of Japan web page
393 (<https://gbank.gsj.jp/seamless/seamless2015/2d>)).

394
395 Figure 2 PPL thin section images and their traced counterparts. (a) & (b) Poly-cataclasites with
396 foliated clasts embedded within randomly oriented cataclasite; (c) & (d) Poly-cataclasites with
397 randomly oriented clasts embedded with foliated cataclasites; (e) & (f) C'-S fabric formed by the
398 pressure solution seams of a foliated cataclasites, indicating a north side to the west sense of shear.

399
400 Figure 3 Graph showing the mineral percentage of the samples collected in the location indicated
401 in **Fig 1**, while the highlighted sample names represent samples collected from the cataclasite
402 zones.

403
404 Figure 4 SEM-EDS elemental mapping of cataclasite sample G.myl 2. (a) Electron back scattered
405 image; (b) Image of all combined elements labeled with respective minerals. Ab: Albite, Qtz:
406 Quartz and Ms: Muscovite; (c) Si elemental map; (d) Al elemental map; (e) Ca elemental map; (f)
407 Na elemental map; (g) Mg elemental map; (h) Fe elemental map; (i) K elemental map.

408
409 Figure 5 Images showing the poly-cataclasite clasts. (a) Plane-polarised thin section image of a
410 poly-cataclasite; (b) An enlargement of a G2 clast by electron backscattered image; (c) Traces of
411 the perimeter of the G2 clast from (a); (d) Image showing the traces of the perimeter of G1 clast.

412
413 Figure 6 (a) & (b) Scattered plot of Rf/Φ for G1 and G2 clasts respectively. The red dot represents
414 the mean Rf value. (c) & (d) Fry's plot based on the G1 and G2 clast respectively. The red circle
415 represents the area of void.

416

417 Figure 7 (a) Log-log graph of the cumulative probability vs grain diameter showing a power-law
418 distribution for G1 and G2 clast; (b) Scattered plot of the Detection probability of clast fragment
419 vs grain diameter for G1 and G2 clast for indication of fluidisation.

420

421 Figure 8 (a) A suggest model for the development of poly-cataclasites^{13,36,43,44,47-49,51}; (b-e) The
422 evolution of poly-cataclasites. Further explanations available in Conclusions.

Figures

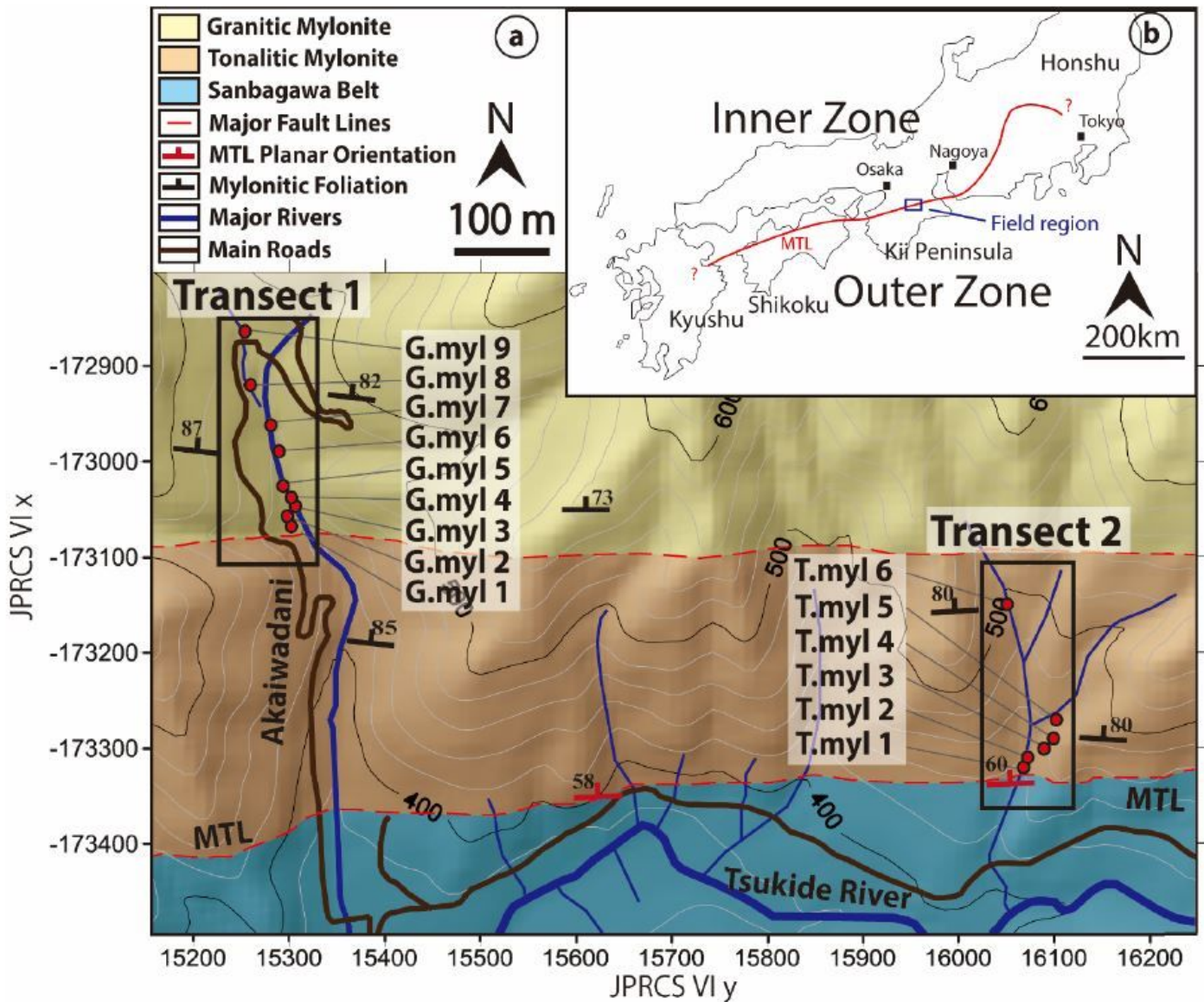


Figure 1

(a) Geological map showing the lithological distribution and location of samples collected in the MTL fault zone. Black and red T-symbols represent the mylonitic foliation and the planar orientation of the MTL respectively. Contours are spaced with a 20 m interval. (b) Map indicating the location of the field region (Source: Geological Survey of Japan web page (<https://gbank.gsj.jp/seamless/seamless2015/2d>)).

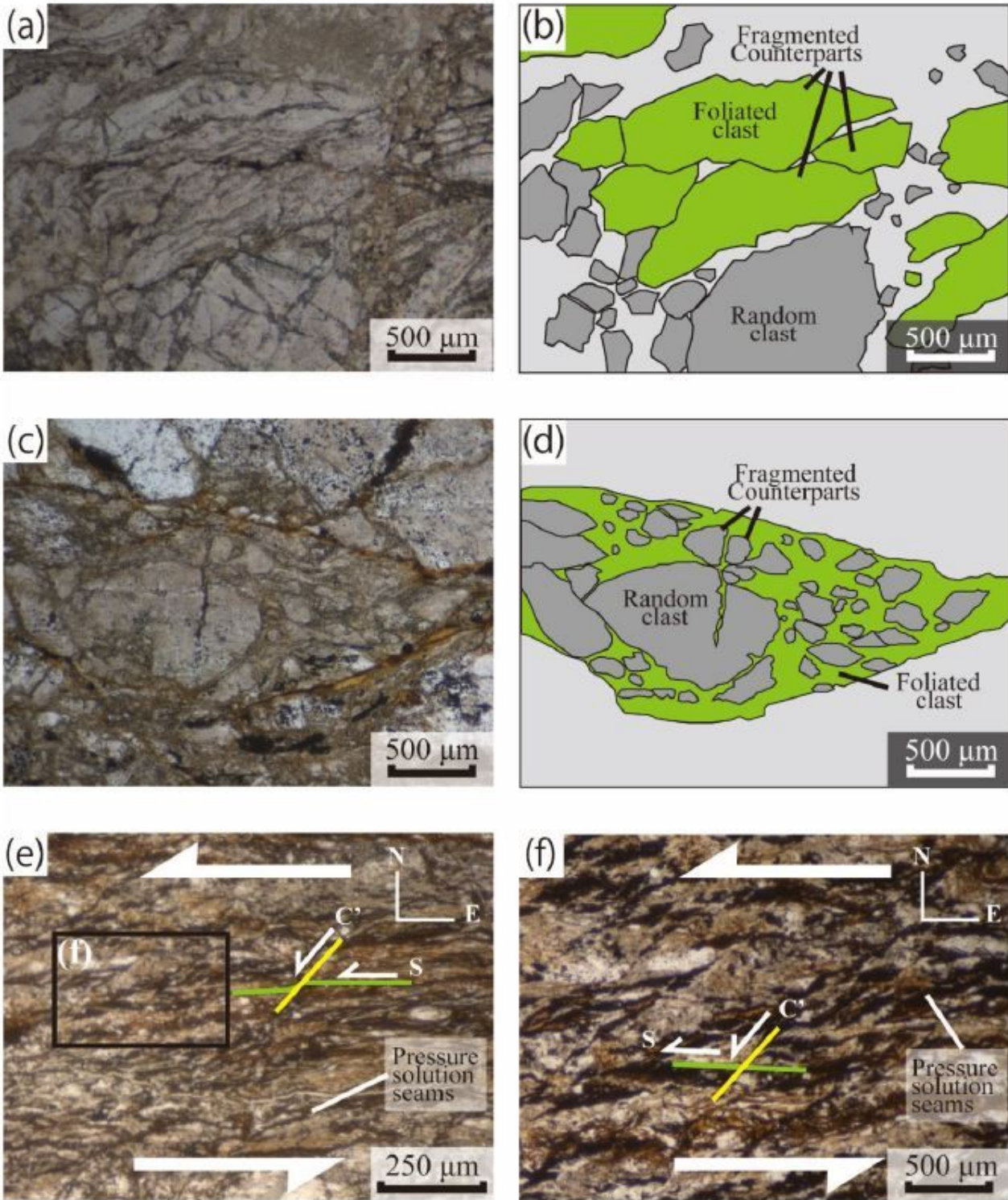


Figure 2

PPL thin section images and their traced counterparts. (a) & (b) Poly-cataclasites with foliated clasts embedded within randomly oriented cataclasite; (c) & (d) Poly-cataclasites with randomly oriented clasts embedded with foliated cataclasites; (e) & (f) C'-S fabric formed by the pressure solution seams of a foliated cataclasites, indicating a north side to the west sense of shear.

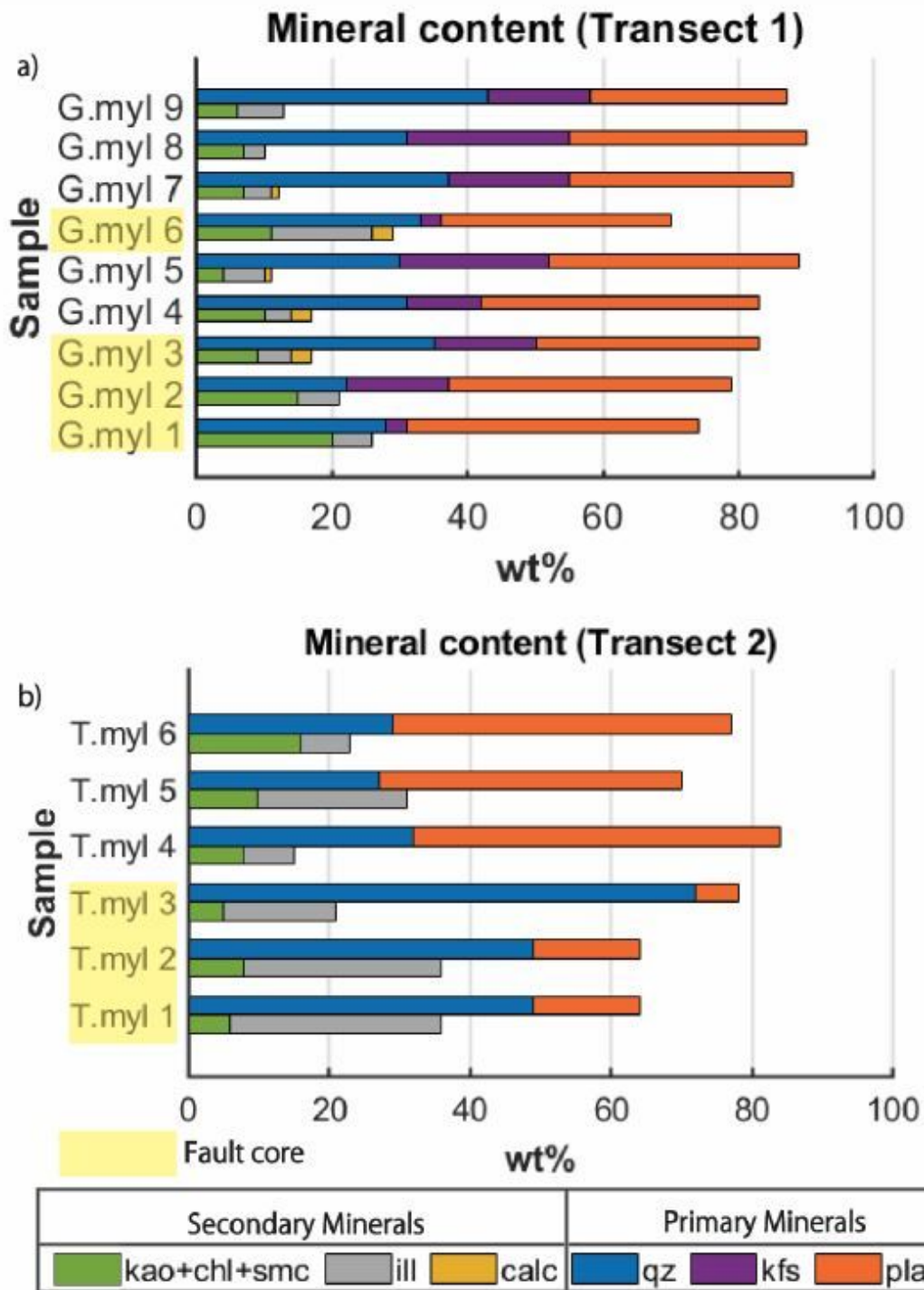


Figure 3

Graph showing the mineral percentage of the samples collected in the location indicated in Fig 1, while the highlighted sample names represent samples collected from the cataclasite zones.

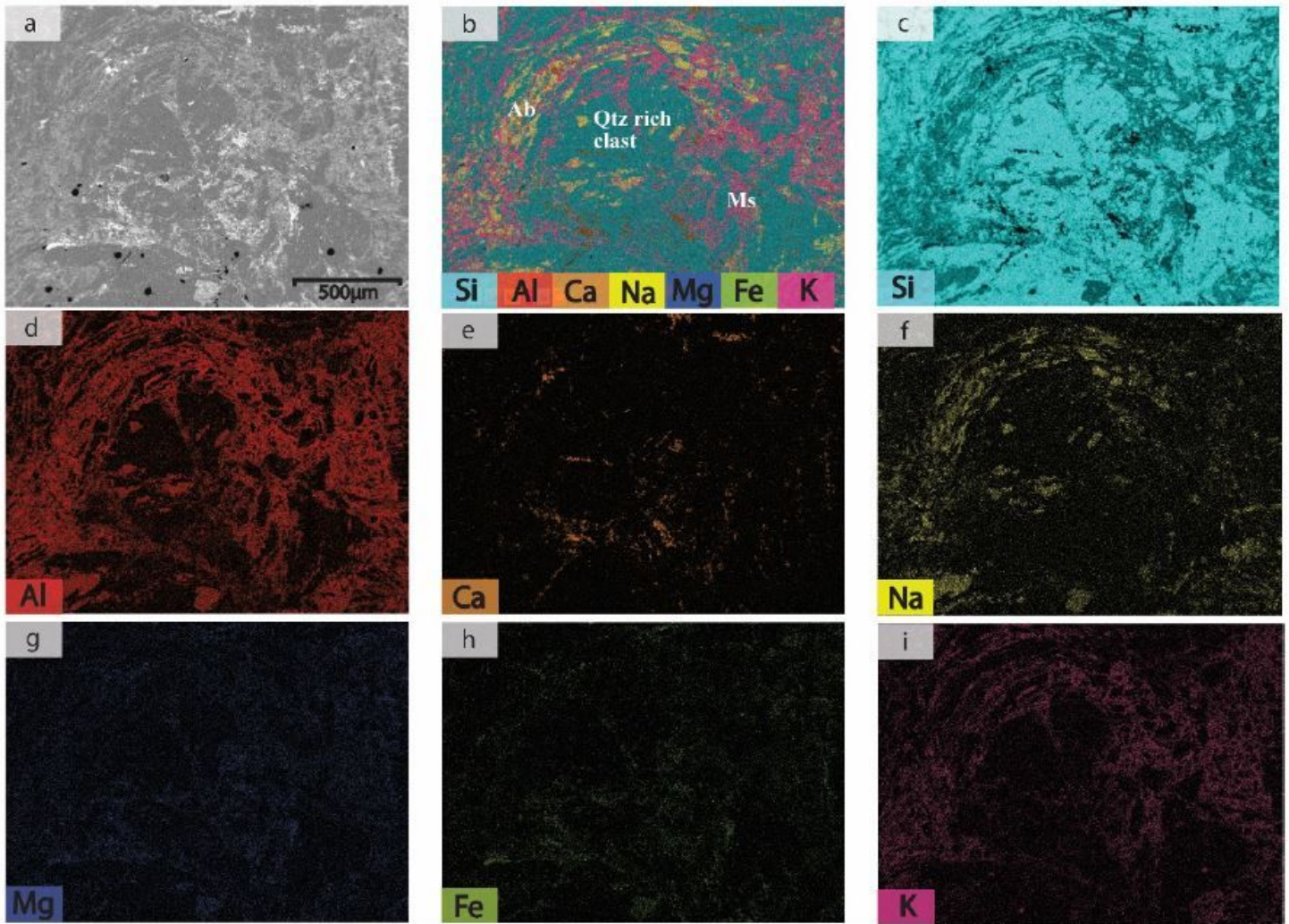


Figure 4

SEM-EDS elemental mapping of cataclasite sample G.myl 2. (a) Electron back scattered image; (b) Image of all combined elements labeled with respective minerals. Ab: Albite, Qtz: Quartz and Ms: Muscovite; (c) Si elemental map; (d) Al elemental map; (e) Ca elemental map; (f) Na elemental map; (g) Mg elemental map; (h) Fe elemental map; (i) K elemental map.

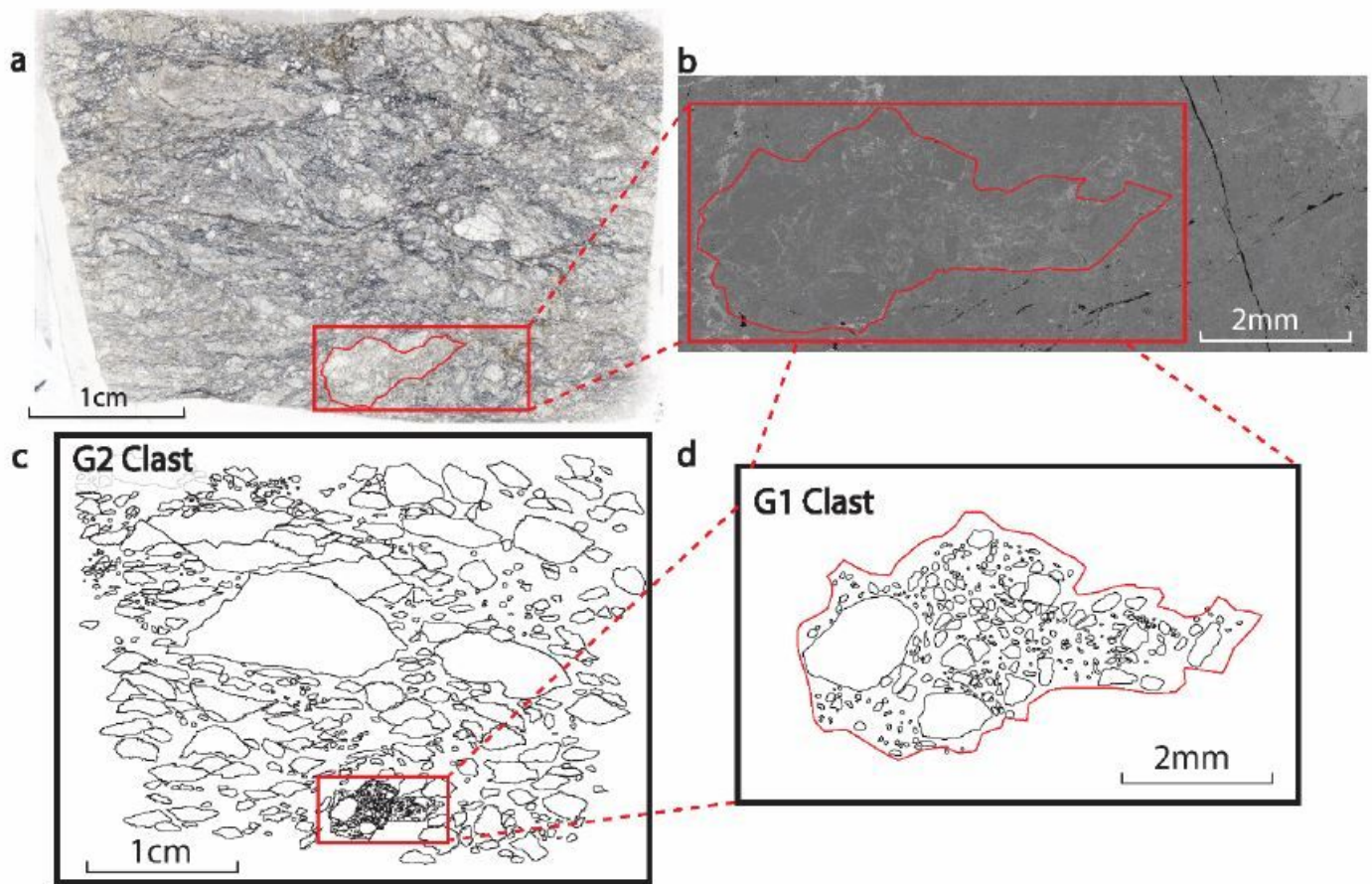


Figure 5

Images showing the poly-cataclasite clasts. (a) Plane-polarised thin section image of a poly-cataclasite; (b) An enlargement of a G2 clast by electron backscattered image; (c) Traces of the perimeter of the G2 clast from (a); (d) Image showing the traces of the perimeter of G1 clast.

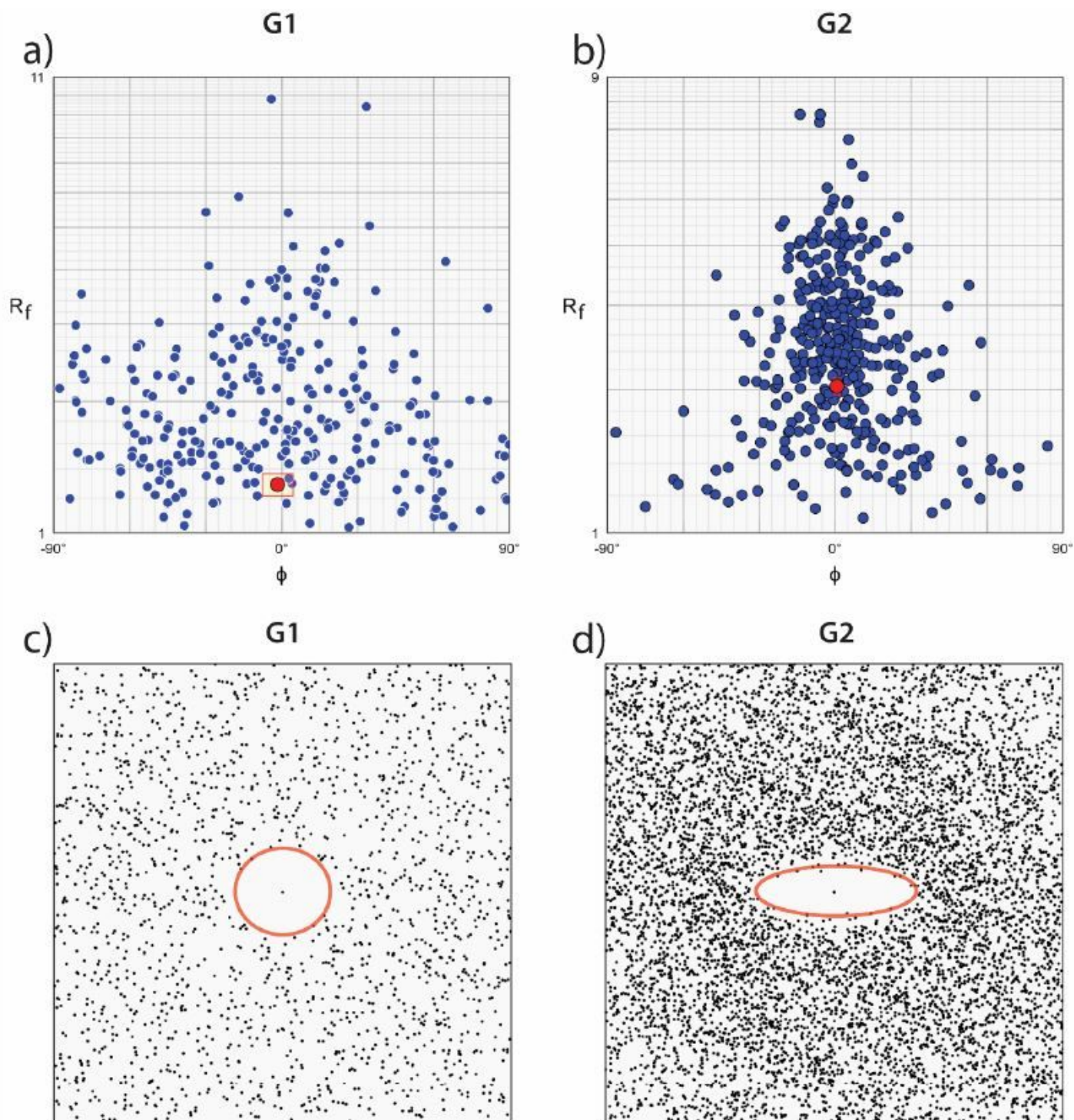


Figure 6

(a) & (b) Scattered plot of R_f/Φ for G1 and G2 clasts respectively. The red dot represents the mean R_f value. (c) & (d) Fry's plot based on the G1 and G2 clast respectively. The red circle represents the area of void.

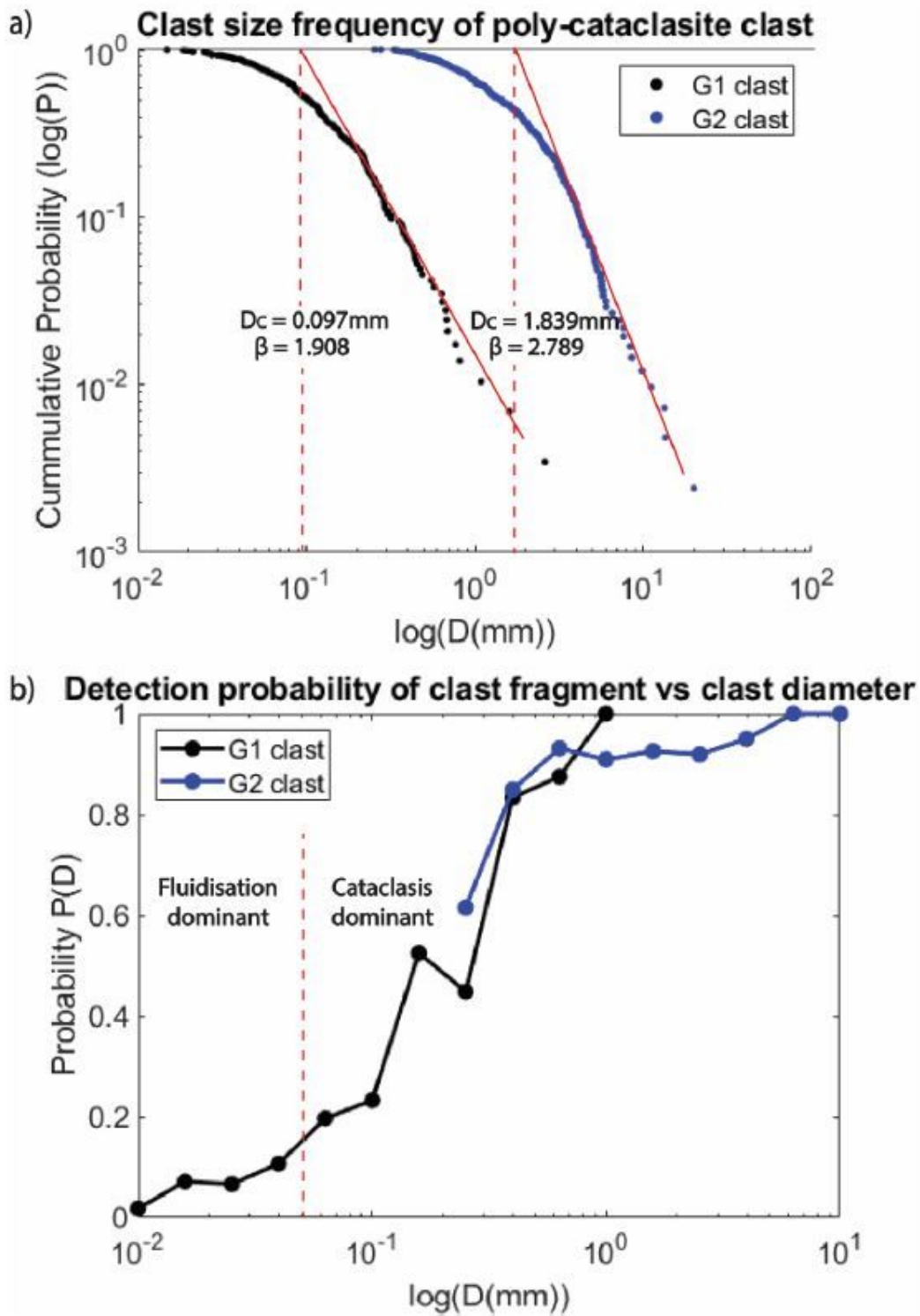


Figure 7

(a) Log-log graph of the cumulative probability vs grain diameter showing a power-law distribution for G1 and G2 clast; (b) Scattered plot of the Detection probability of clast fragment vs grain diameter for G1 and G2 clast for indication of fluidisation.

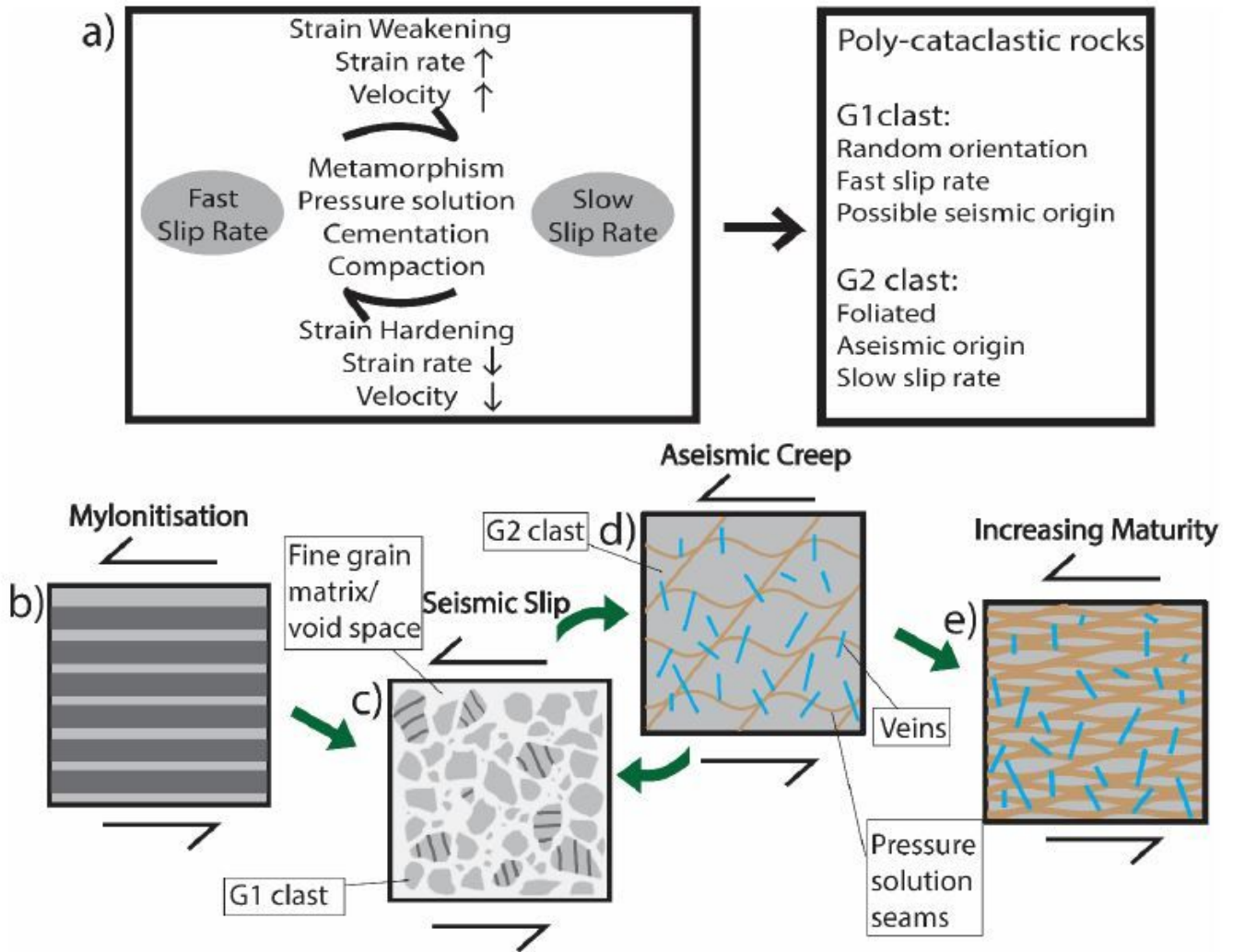


Figure 8

(a) A suggest model for the development of poly-cataclasites^{13,36,43,44,47–49,51}; (b-e) The evolution of poly-cataclasites. Further explanations available in Conclusions.